Charge-dependent interactions of monomeric and filamentous actin with lipid bilayers

Carsten F. E. Schroer[a,b], Lucia Baldauf[c,d], Lennard van Buren[c,d], Tsjerk A. Wassenaar[a,b], Manuel N. Melo[e], Gijsje H. Koenderink[c,d,1], and Siewert J. Marrink[a,b,1]

[a]Groningen Biomolecular Sciences and Biotechnology Institute, University of Groningen, 9747 AG, Groningen, The Netherlands; [b]Zernike Institute for Advanced Materials, University of Groningen, 9747 AG, Groningen, The Netherlands; [c]Department of Bionanoscience, Kavli Institute of Nanoscience Delft, Delft University of Technology, 2629 HZ Delft, The Netherlands; [d]Living Matter Department, AMOLF, 1098 XG Amsterdam, The Netherlands; and [e]Instituto de Tecnologia Química e Biológica, New University of Lisbon, 2780-157, Oeiras, Portugal

Edited by Michael L. Klein, Temple University, Philadelphia, PA, and approved February 4, 2020 (received for review August 27, 2019)

The cytoskeletal protein actin polymerizes into filaments that are essential for the mechanical stability of mammalian cells. In vitro experiments showed that direct interactions between actin filaments and lipid bilayers are possible and that the net charge of the bilayer as well as the presence of divalent ions in the buffer play an important role. In vivo, colocalization of actin filaments and divalent ions are suppressed, and cells rely on linker proteins to connect the plasma membrane to the actin network. Little is known, however, about why this is the case and what microscopic interactions are important. A deeper understanding is highly beneficial, first, to obtain understanding in the biological design of cells and, second, as a possible basis for the building of artificial cortices for the stabilization of synthetic cells. Here, we report the results of coarse-grained molecular dynamics simulations of monomeric and filamentous actin in the vicinity of differently charged lipid bilayers. We observe that charges on the lipid head groups strongly determine the ability of actin to adsorb to the bilayer. The inclusion of divalent ions leads to a reversal of the binding affinity. Our in silico results are validated experimentally by reconstitution assays with actin on lipid bilayer membranes and provide a molecular-level understanding of the actin–membrane interaction.

actin cytoskeleton | protein–lipid interactions | coarse-grained molecular dynamics | biological soft matter | artificial cell cortex

Actin is a globular protein that is the most abundant protein in mammalian cells, often accounting for 10% or more of total protein (1). The importance of actin arises from the ability of actin monomers (G-actin) to polymerize into filaments of micron-length scale (F-actin) that are one of the main constituents of the cytoskeleton and fulfill many roles (2–4): located under the surface of the plasma membrane, actin filaments, together with the contractile protein myosin, form a cortical network that is responsible for shape and mechanical stability of the cell surface (5, 6). Meanwhile, branched actin structures push against the membrane and drive cell migration (7).

For all of these purposes, actin has to interact with lipid membranes, and a number of in vitro studies have tried to elucidate the nature of actin–membrane interactions (8–10). One central outcome of these studies is the importance of the presence of charged lipids for the ability of actin filaments to adsorb directly to the membrane: F-actin generally does not adsorb to bilayers consisting only of neutral lipids, or partially of negatively charged lipids (10–12), consistent with the overall negative charge of actin filaments (13). In contrast, positively charged lipid mono- and bilayers are not only able to adsorb the filaments (8, 14–16) but can even catalyze the formation of F-actin (8, 15) and form stacked hierarchical structures (17).

Other in vitro experiments have shown, however, that actin can in fact interact with neutral or negatively charged bilayers (9, 10, 18). This contradiction may be reconciled by considering the presence of divalent ions, calcium or magnesium, in the buffer. There is strong experimental evidence that divalent ions can reverse the adsorption properties of lipid bilayers (9, 10), which is reminiscent of divalent ions acting as a molecular glue that allows F-actin to form bundles (19–22). A systematic evaluation of actin–membrane binding with respect to both bilayer composition and ion concentration is so far lacking.

In vivo, the actin cortex resides close to the cytosolic leaflet of the plasma membrane, which is negatively charged, mainly due to the presence of phosphatidylserine lipids (23). The linkage between the cortex and the membrane is thus realized by linker proteins, for example, the ERM proteins Ezrin, Radixin, and Moesin (24, 25), which can simultaneously bind to the membrane and the actin filaments. The mechanism of this binding is rather complex and depends on posttranslational alterations of the binding protein (26, 27) as well as the composition of the membrane (28–31). Divalent ions are ubiquitous in cells. The majority of these ions are calcium, with a concentration range of 0.1 to 1.0 μM in the cytosol (32), although the concentration near the negatively charged inner leaflet can be much higher due to the high binding affinity of Ca^{2+} to anionic membranes (33, 34). Interestingly however, calcium-mediated direct

Significance

Actin filaments are biopolymers that reside close to the plasma membrane in mammalian cells and are essential for its mechanical stability and shape. In vitro experiments have demonstrated that direct interactions between actin strands and lipid membranes exist and that the lipid composition and the ions in the buffer are of major importance. Here, we utilize molecular dynamics simulations to systematically analyze these effects on a close-to-atomistic resolution. We find that the charge of the lipid membrane determines the attraction/repulsion of the actin filaments, which can be reversed by the inclusion of divalent buffer ions. Our results are verified by an experimental reconstitution assay. These results suggest that direct actin binding can be used for engineering synthetic cells.

Author contributions: C.F.E.S., G.H.K., and S.J.M. designed research; C.F.E.S., L.B., L.v.B., T.A.W., and M.N.M. performed research; C.F.E.S., L.B., and L.v.B. analyzed data; and C.F.E.S., L.B., G.H.K., and S.J.M. wrote the paper.

The authors declare no competing interest.

This article is a PNAS Direct Submission.

Data deposition: The parameters for the molecular dynamics simulations are provided under "Actin with ADP and ATP" at http://cgmartini.nl/index.php/example-applications2/peptides.

[1]To whom correspondence may be addressed. Email: g.h.koenderink@tudelft.nl or s.j.marrink@rug.nl.

This article contains supporting information online at https://www.pnas.org/lookup/suppl/doi:10.1073/pnas.1914884117/-/DCSupplemental.

First published March 2, 2020.

adsorption of actin filaments to the membrane has not been observed. There is evidence that cells couple the down-regulation of divalent cation concentration and F-actin networks, especially near the lipid bilayer. For example, the presence of F-actin is able to deactivate Ca^{2+} pumps (35), and higher than usual divalent ion concentrations can activate actin-severing and -capping proteins (32, 36). Similar effects can be observed for magnesium ions as well (37). However, why the colocalization of F-actin and divalent cations is suppressed by cells has not been well studied. Moreover, direct interactions between actin, divalent ions, and lipid membranes have not been characterized in molecular detail, despite growing evidence that buffer ion valence and lipid composition significantly alter actin filament dynamics in in vitro-supported lipid-bilayer experiments. The present work sets out to characterize the interactions between actin, divalent cations, and lipid membranes as a means to better understand their potential effects on actin-mediated cellular functions. Furthermore, an in-depth knowledge of these processes can be used as a design principle in biology-inspired build-up and control of artificial cell cortices (38, 39) that can be applied in the construction of synthetic cells.

Molecular dynamics (MD) simulations are a valuable tool to analyze these kinds of questions by offering detailed information on molecular time and length scales. Both G- and F-actin have frequently been simulated with respect to their dynamics and structural properties during actin polymerization (40–48). Simulations on an atomistic resolution are limited, however, to time scales of typically hundreds of nanoseconds, which may not be enough to study the processes relevant for actin–membrane interactions. Supra–coarse-grained (CG) simulations on the other hand, in which a single actin unit is represented by few beads, have been successfully applied to study the mechanical properties of F-actin (49–51) but cannot be easily combined with other cellular components. The Martini force field (52, 53) is a CG model that is located between the atomistic and the supra-CG resolution by combining on average four nonhydrogen atoms into one CG particle. It is one of the most frequently used CG force fields and has been used to model a large variety of membrane-related systems (54, 55). Furthermore, there exist extensions for protein filaments (56) and, recently, cytoskeletal components (57, 58) in this framework.

Here, we use the Martini force field to combine lipid bilayers with a newly parameterized model of G- and F-actin to study the interactions between these components. The actin monomers explicitly contain both adenosine triphosphate (ATP) and a posttranslational modification, a methylation at His73, that is abundant in many actin variants (59). The main goal of this work is to understand the influence of lipid composition, in particular, with respect to the net charge, and the nature of the ions in the buffer, monovalent or divalent, on the process of actin binding to the lipid bilayers. Furthermore, we compare the behavior of monomeric and filamentous actin to obtain insights into potential mechanisms of actin filament formation near lipid bilayers. To validate the simulation results, we conducted an experimental study of actin filaments interacting with supported lipid bilayers in a flow-chamber setup. In analogy to the simulations, we systematically varied both the composition of the bilayer and the nature of the buffer ions and observed a good agreement between in silico and in vitro data.

Results

Adsorption Behavior of F-Actin to Differently Charged Lipid Bilayers. To study the interaction of F-actin with lipid membranes, we placed an infinite filament next to a lipid bilayer patch. A substantial water layer of around 2 nm initially separates the filament from the membrane surface. The bilayers consisted either completely (100%) of the zwitterionic lipid 1-palmitoyl-2-oleoyl-*sn*-glycero-3-phosphatidylcholine (POPC100) without a net charge or partially (20%) of either the anionic lipid 1-palmitoyl-2-oleoyl-*sn*-glycero-3-phosphatidylserine (POPS20) or the cationic lipid 1-palmitoyl-2-oleoyl-3-trimethylammonium-propane (POTAP20). A snapshot of the simulation setup can be found in *SI Appendix*, Fig. S7.

In Fig. 1*A*, the minimum distance between the actin filament and POPC100, POPS20, and POTAP20 is shown, beginning from the start of the simulations. We define the minimum distance as the shortest of all of the distances between the beads of the protein and the lipid head groups. The minimum distances decrease in the early stages of the simulation from around 2 nm to values below 1 nm, independent from the lipid composition. The reason for this initial decay is the preparation of the system: during the equilibration, both the filament and the bilayer were restrained by harmonic potentials (*Computational Methods*) that kept them in a stretched state. After release of the restraints, the filament and the bilayer began to buckle, and hence the minimum distance between them decreased. However, qualitative differences can be observed in the way F-actin interacts with the bilayer: for POPS20, one detects strong fluctuations of the minimum distance and even significant detachment from the bilayer, e.g., in run 3 (light blue line) at 600 ns. In contrast, the filaments bind very stably to POTAP20 after 200 ns and display almost no fluctuations in their minimum distance to the head groups of the bilayer. In the case of POPC100, the situation is somewhat in between: the filaments interact with the membrane, but no stable binding mode is obtained.

To study the interactions with the different membranes more quantitatively, we computed the contour lines of both the bilayer and the filament. For this purpose, the average z positions, i.e., the centers of mass, of the lipids of the bilayer and the backbone beads of the actin were determined at a particular x coordinate and averaged over the last 200 ns of the simulation runs. Please note that, while the minimum distance measures the closest surface-to-surface distance between the filament and the bilayer at a certain point in time (Fig. 1*A*), the contour line represents a time average of the center-to-center distance. The graphs are shown, next to representative snapshots, in Fig. 1*B*. The contour of the filament displays some regular fast oscillations (wavelength, ~ 5 nm), which reflect the helical nature of the protein filament. To quantify the adsorption of F-actin to the bilayer, the average height between the filament and the bilayer was measured. These values confirm trends that were already observed for the minimum distance: F-actin approaches POTAP20 the closest ($\langle dz \rangle = 6.70 \pm 0.13$ nm), whereas the distance to POPC100 ($\langle dz \rangle = 7.36 \pm 0.18$ nm) and POPS20 ($\langle dz \rangle = 8.37 \pm 0.47$ nm) is significantly larger. Thus, the negatively charged actin filament tightly binds to the positively charged POTAP20, whereas it remains further apart from the neutral POPC100. The difference in distance between POPC100 and POPS20 furthermore implies a slight repulsion from POPS20 due to the presence of anionic lipids.

Another aspect of the actin–lipid interactions is the relationship between the curvatures of the filament and the bilayer. In Fig. 1*C*, the contour lines of one example run for each bilayer, the same as used in Fig. 1*B*, are shown where the contours of the filament are shifted by the average z distance between the filament and bilayer. Clearly, the curvatures of F-actin and POPC100 are very similar, whereas the contour lines of the filament and POPS20 are significantly different. In the case of POTAP20, as already suggested by the snapshot from the end of the simulations in Fig. 1*B*, the curvatures of the bilayer and the filament closely match, thereby reflecting the shape control due to the interaction between filament and bilayer. The dissimilarity between the contour of actin and POPS20 suggests only weak interactions between both since they are not able to significantly influence each other's profile. The different behavior

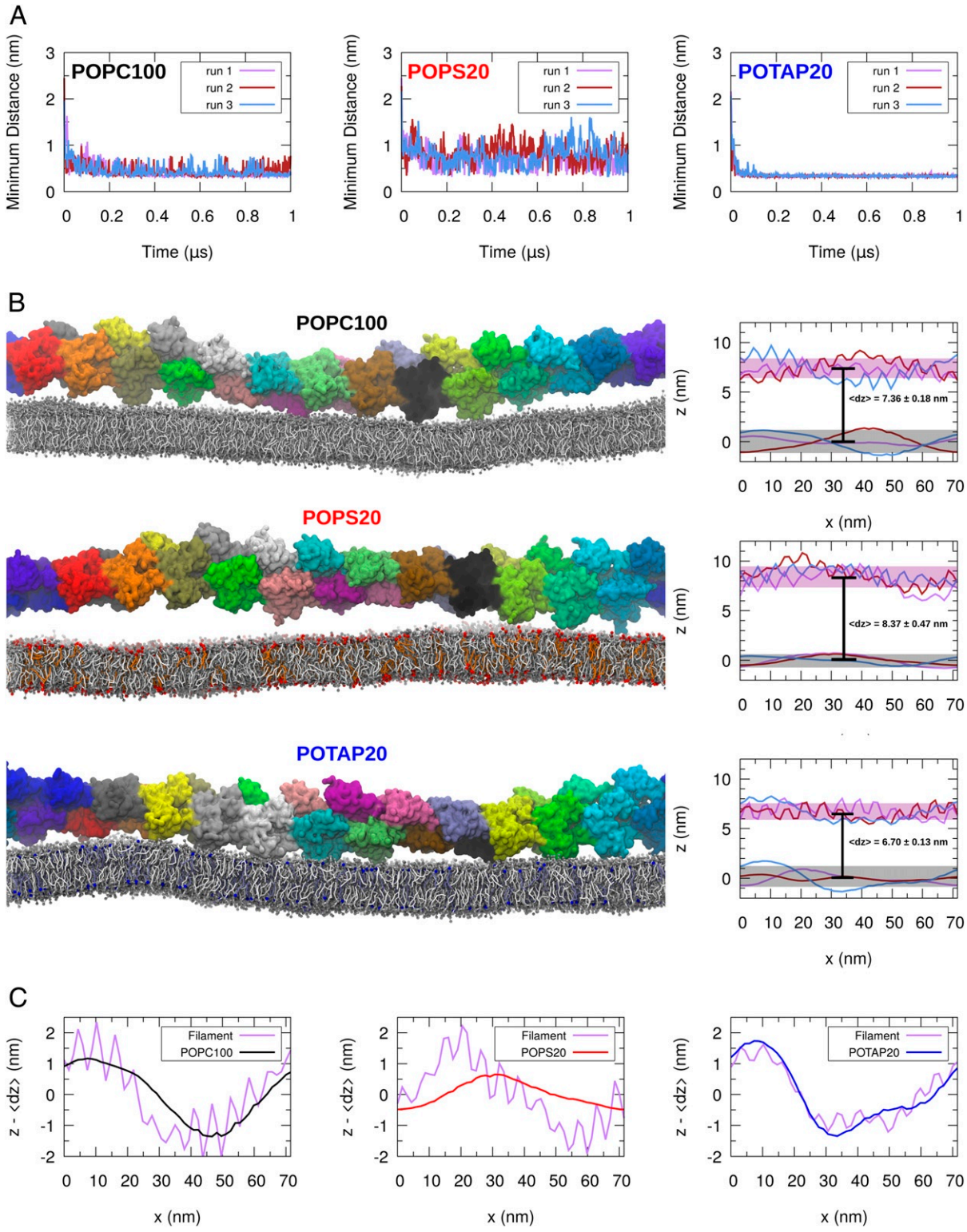

Fig. 1. Results of the F-actin simulations. (*A*) Minimum distances of the filament to the head groups of the lipid bilayer as a function of time. The line colors refer to the different replicas of the simulations. (*B*, *Left*) Representative snapshots from the end of the simulations. (*B*, *Right*) Contour of the filament (highlighted in purple) and the bilayer (highlighted in gray), averaged over the last 200 ns of the simulation. The colors of the contour lines refer to the different replicas (*A*); the diameter of the transparent bars indicates the fluctuations around the mean. (*C*) Contour lines of representative replicas. The lines of the filaments were shifted by the average distance $\langle dz \rangle$ between filament and membrane (*B*).

of POPC100 and POPS20 could be caused by two effects: either the presence of anionic lipids prevents the transfer of the actin undulations to the lipid bilayer or the increased distance between filament and membrane is the limiting factor. To clarify this aspect, we conducted an additional set of simulations of F-actin and POPC100, where $\langle dz \rangle$ was restrained

to 7.5, 8.0, and 8.5 nm (*SI Appendix*, Fig. S3). We can thereby observe that an increasing separation (above 7.0 nm) leads to stronger differences of contour lines as the filament cannot effectively attach to the bilayer anymore. This implies that there is, rather independent from the exact composition, a critical average z distance of above 7.5 nm, beyond which the undulations of actin do not (greatly) influence the fluctuations of the bilayer anymore.

Interaction of G-Actin with Differently Charged Bilayers. For the simulation of G-actin, a single actin monomer was placed next to a lipid bilayer patch (*SI Appendix*, Fig. S7*B*). The compositions of the bilayers were the same as for the F-actin simulations. Again, we computed the minimum distance between G-actin and the head groups of the different bilayers (Fig. 2*A*). The trends for the actin monomers are similar to those of the actin filaments: G-actin shows a strong affinity to the positively charged POTAP20, whereas it stays more distant from POPS20. The situation with POPC100 is again in between but resembles more the interaction with POPS20. Interestingly, there are striking qualitative differences in the adsorption dynamics between the monomers and the filaments: whereas the minimum distances of the filaments display some fluctuations, whereby the magnitude depends on the type of bilayer, in each case, F-actin resides close to the bilayer. G-actin, on the contrary, shows many binding and unbinding events. This is even true for POTAP20. Our observation is in agreement with fluorescence measurements of actin next to cationic monolayers, which revealed no detectable adsorption of G-actin to the membrane but strong binding of F-actin (16). The binding dynamics are thus much more transient for G-actin, in contrast to the rather static interaction between F-actin and the lipid bilayers.

In Fig. 2*B*, the protein densities, averaged over the last 9 μs of the simulation, are shown relative to the normal of the lipid bilayers (indicated as green and gray areas). Please note that, due to the periodic boundary conditions, actin can access the bilayer from both sides. The actin monomer remains distant from POPC100 (average: 6.38 nm) and POPS20 (average: 6.46 nm); the exact values may not be meaningful, however, since they are likely determined by the finite size of the simulation box. The density distribution of POPC100 is slightly wider than that of POPS20 (which can also be seen by the lower maximum of the normalized density distribution), which reflects that G-actin can approach POPC100 slightly closer, hence indicating a somewhat higher affinity of G-actin to the neutral than to the negatively charged bilayer. The highest affinity can be observed for POTAP20: here, G-actin resides at an average distance of 5.67 ± 1.33 nm.

As G-actin is roughly rectangular in shape, it contains two major surfaces: the "front" surface, where the amino terminus (N terminus) is located, and the opposing "back" surface (Fig. 2*B*, *Right*). To determine whether one of these surfaces preferentially binds to the bilayer, we computed the relative number of binding events for each side. We define a binding event as an event in which the minimum distance between the protein and the bilayer is < 0.75 nm; the choice of a smaller cutoff does not significantly change the statistics. The results of the analysis are shown in Fig. 2*B*, *Right*. In agreement with the observations in Fig. 2*A*, G-actin adsorbs to POTAP20 much more often than to any of the other lipid bilayers. More than 80% of the binding events occur via the front of actin. Of particular importance is the polyanionic N terminus of actin (residues 1 to 4; sequence: DEDE), which is involved in 20% of binding events. The N terminus attaches to the surface of the membrane and inserts only weakly in the head group region of POTAP20 (*SI Appendix*, Fig. S4*A*). The difference between the front and the back side is less pronounced with POPC100 or even slightly reversed in the case of POPS20. For both of these membranes, the N terminus does not play a significant role during the adsorption events. In *SI Appendix*, it is shown that the same trends can be observed for adenosine diphosphate (ADP)-containing monomers as well (*SI Appendix*, Fig. S4*B*). The adsorption of actin to POTAP20 and the depletion from POPS20 is, however, slightly less pronounced, which is in line with the less negative net charge of the protein.

To explore the dependence of the adsorption behavior to cationic membranes on the charge density, we performed 10 replicas of POPC bilayers that contain either 10, 20, or 40% POTAP (*SI Appendix*, Fig. S5*A*). For all concentrations, the transient nature of the G-actin adsorption remains. In some occasions, especially for 40% POTAP, we could observe a more stable binding mode that persisted for several microseconds. In this conformation, G-actin adsorbs via the "flap" (residues 236 to 251) to the bilayer and exposes its barbed end to the buffer; a snapshot can be seen in *SI Appendix*, Fig. S5*B*. We note, however, that although this conformation is rather persistent on the time scale of our simulations, the adsorption is still reversible.

Influence of Divalent Ions on the Actin–Bilayer Interactions. In order to explore whether the buffer cations influence the interactions between actin and the bilayers, we performed additional simulations where the 150 mM KCl solution was replaced by 75 mM $MgCl_2$, therefore keeping the total number of positive charges in the buffer constant. The minimum distances between G-actin and the bilayer are shown in Fig. 2*C*. For POPC100Mg75, the interaction between the protein and the bilayer is very similar to the case with 150 mM KCl, although it appears that, indicated by the slightly increased average value of the minimum distance compared to Fig. 2*A*, G-actin is slightly less attracted by the bilayer. The same holds for POPS20Mg75, to which G-actin does not adsorb. The biggest differences can be observed for POTAP20Mg75: whereas the actin monomer had a clear tendency to remain close to POTAP20 in the presence of KCl, it shows no affinity to the bilayer in the presence of $MgCl_2$ whatsoever. The divalent ions thus inhibit the attraction of the negatively charged actin to the positively charged membrane.

To explore the differences due to the buffer ions in solution in more detail, we computed the radial distribution of cations around the protein for both types of ions (Fig. 2*D*). There, striking differences become apparent: whereas K^+ only shows a weak affinity to G-actin, one can observe a high density of Mg^{2+} around the protein. In particular, we observe that the affinity of divalent ions to the N terminus is massively increased as compared to the affinity of the monovalent ions (*SI Appendix*, Fig. S4*C*). In the case of POTAP20, where we observed the interaction with the negatively charged N terminus to be critically important for membrane binding, this accumulation of Mg^{2+} impairs actin adsorption. In the case of POPS20, on the other hand, the cationic shell is much less pronounced because G-actin competes with the negative charges of the bilayer for the magnesium ions. Hence, an inversion of the electrostatic properties, as it is observed for the system with POTAP20, cannot be achieved.

Finally, we performed a single simulation of F-actin for each bilayer in the presence of $MgCl_2$ to explore how the trends detected for the monomers transfer to the filaments. Snapshots from the end of these simulations as well as their (shifted) contour line along the x axis are shown in Fig. 3*A*. For POPC100Mg75 and POTAP20Mg75, the simulations are in agreement with what has been observed for the monomers: F-actin cannot attach to POPC100 nor POTAP20 in the presence of divalent ions, and the curvatures of filament and bilayer are distinctly different. For POPS20Mg75, however, the filament can adsorb to the bilayer and adjust its shape. The reason for the

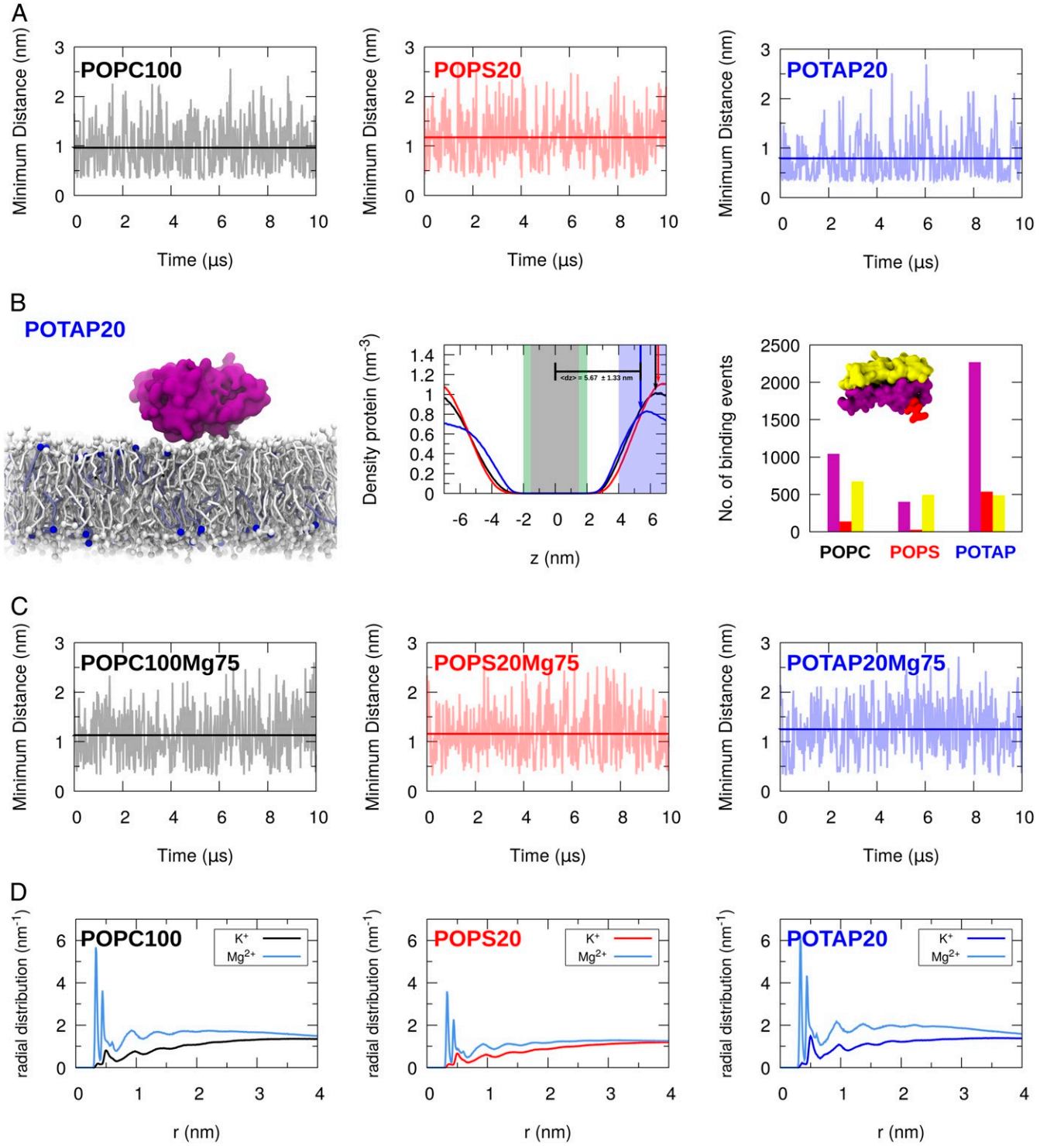

Fig. 2. Results of the G-actin simulations. (*A*) Minimum distances of the actin monomer to the head groups of the lipid bilayer as a function of time. The solid lines indicate the average values. (*B*, *Left*) Representative snapshot of G-actin interacting with POTAP20 from the end of the simulation. (*B*, *Middle*) G-actin density with respect to the bilayer normal, averaged over the last 9 μs of the simulation. The colors of the lines refer to the simulations with POPC100 (black), POPS20 (red), and POTAP20 (blue), respectively. The blue area indicates the mean fluctuations of the actin density around the average. The green area represents the head group region of the bilayer, the gray area the center of the lipid bilayer. (*B*, *Right*) Statistics of the binding events (minimum distance < 0.75 nm). *Inset* depicts the defined surfaces (in purple and yellow) and the N terminus within the front surface (red). (*C*) Minimum distances of the actin monomer to the head groups of the lipid bilayer as a function of time for the simulations containing 75 mM $MgCl_2$. The solid lines indicate the average values. (*D*) Radial distribution function of cations around G-actin for 150 mM KCl (black, red, and blue) and 75 mM $MgCl_2$ (light blue).

adsorption to POPS20 can be found in the distribution of Mg^{2+} around the filaments Fig. 3*B*: we find that magnesium prefers to reside next to anionic residues of the filament thereby screening their negative charges. This behavior is not observed for K^+, which displays a much weaker affinity to actin than Mg^{2+} (Fig. 2*D*). Furthermore, cations (roughly 8.5 Mg^{2+} ions per

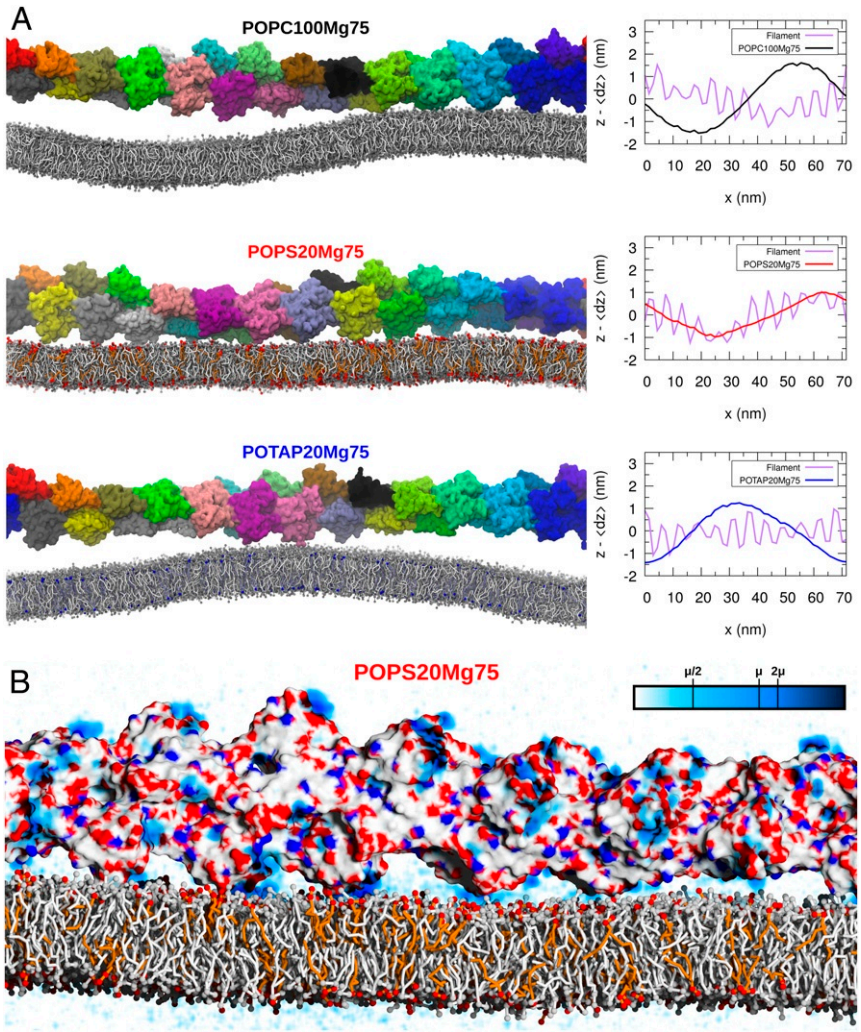

Fig. 3. F-actin interacting with the different bilayers in the presence of 75 mM $MgCl_2$. (*A*, *Left*) Representative snapshots from the end of the simulations. (*A*, *Right*) Contour lines of the filament (purple) and the bilayers (black, red, and blue). The contour lines of the filament have been shifted by the average distances $\langle dz \rangle$ between the filament and the respective bilayer. (*B*) Interaction between F-actin and POPS20 in the presence of magnesium ions. The anionic and cationic residues of F-actin are shown in red and dark blue, respectively. The density of Mg^{2+}, averaged over the last 200 ns, is shown in shades of marine, going from light to dark.

nanometer of filament) are accumulated in between the filament and the bilayer, hence effectively acting as molecular glue. This behavior of magnesium bridging between two negatively charged groups is reminiscent of the mechanism of Ca^{2+}-induced fusion of negatively charged bilayers (60). In summary, we observe that the presence of divalent ions allows to reverse the affinity of actin filaments to the membrane by inhibiting adsorption to POPC100 and POTAP20 but facilitating the attachment of F-actin to POPS20.

Experimental Validation. To test the predictions from the simulations, we performed flow-chamber experiments (Fig. 4*A*): F-actin was polymerized from purified G-actin in different buffer conditions, which varied only in salt concentration and valency (5, 50, or 100 mM KCl or 2.5, 25, or 50 mM $MgCl_2$, respectively) and flowed into channels containing supported lipid bilayers of different lipid composition (100% 1,2-dioleoyl-*sn*-glycero-3-phophocholine [DOPC100], 20% 1,2-dioleoyl-*sn*-glycero-3-phospho-L-serine [DOPS20], 20% 1,2-dioleoyl-3-trimethylammonium-propane [DOTAP20]). Please note that the only difference among the simulated lipids (POPC, POPS, POTAP) is the degree of unsaturation of the lipid tails (fully saturated for PO; monounsaturated for DO lipids), whereas the head groups are the same. We avoided the use of crowding agents, which are often used in reconstitution assays of actin on lipid membranes (61, 62), to prevent depletion-induced unspecific binding of actin to the bilayer.

Fig. 4*B* shows representative total internal reflection fluorescence (TIRF) microscopy images for F-actin interacting with different bilayers in a buffer containing 50 mM KCl (top row) and 25 mM $MgCl_2$ (bottom row). In the case of the buffer with the monovalent ions, we observe a significant coverage only for the DOTAP20 bilayer; both DOPC100 and DOPS recruit hardly any F-actin. Opposite trends can be seen for the $MgCl_2$ buffer: here, the adsorption to the cationic bilayer is greatly reduced as compared to the KCl buffer, and for both the neutral and the anionic bilayer, attached F-actin can be detected.

To get a more quantitative measure of actin adsorption to the supported bilayers in any given condition, we then performed automated image analysis on the TIRF images, where we binarized the pictures and measured the fraction of the surface that was covered with actin filaments. The results of this analysis are displayed in Fig. 4*C*. One can observe two major trends: first, for monovalent ions, only DOTAP20 displays a strong

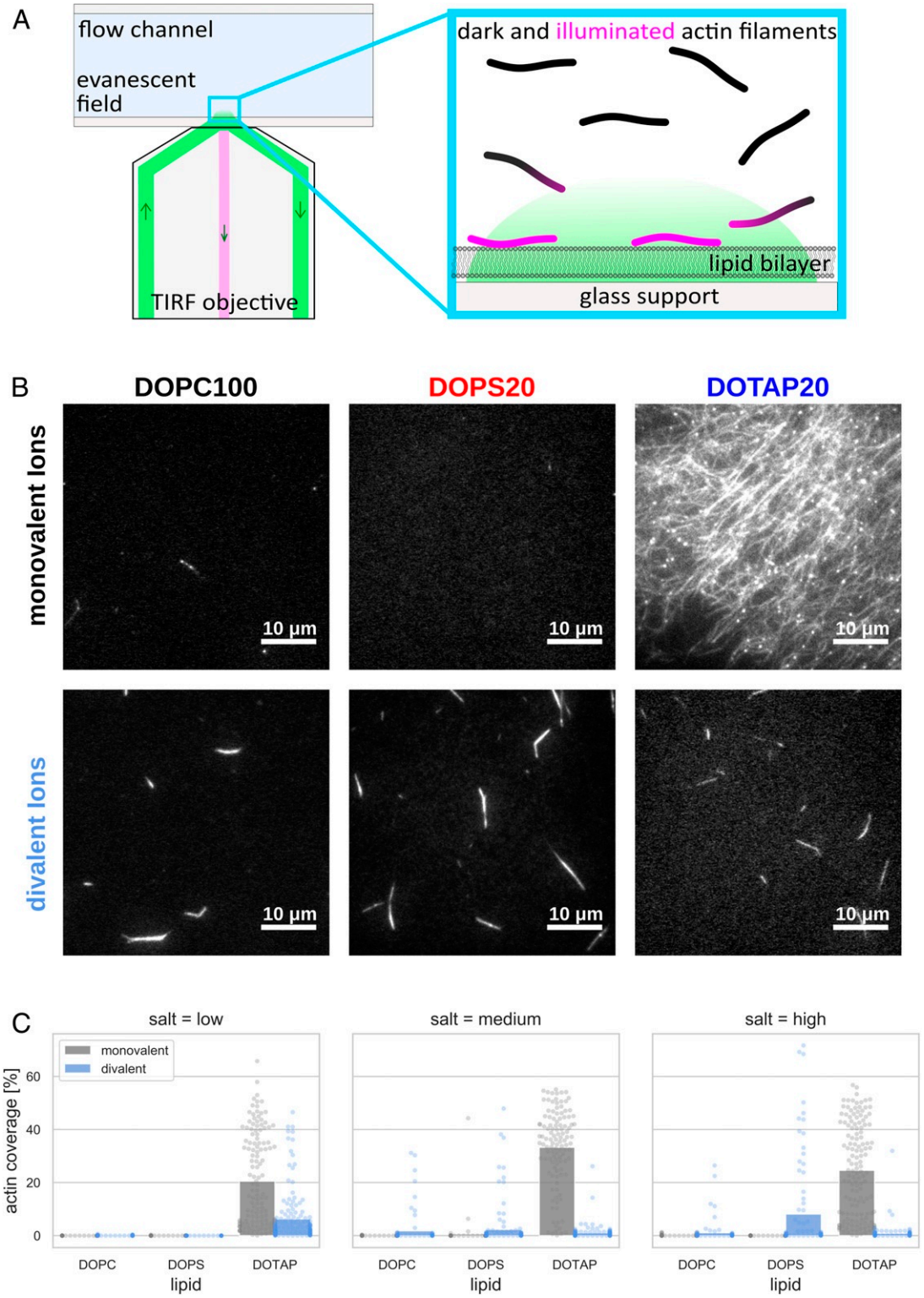

Fig. 4. Results of the flow channel experiments. (*A*) Schematic representation of the experimental setup. (*B*) Representative TIRF images of F-actin interacting with different lipid bilayers. The top row corresponds to F-actin diluted in a buffer with 50 mM KCl, and the bottom row corresponds to a buffer with 25 mM $MgCl_2$. (Scale bars, 10 μm.) (*C*) Quantification of F-actin attached to the lipid bilayers. Each graph corresponds to a different salt concentration (5 mM KCl/2.5 mM $MgCl_2$ [low], 50 mM KCl/25 mM $MgCl_2$ [medium], and 100 mM KCl/50 mM $MgCl_2$ [high], respectively). Each point shows the fraction of membrane area covered with actin in an individual TIRF image. Bars represent the average over the results from all images.

tendency to adsorb actin filaments. DOPC100 and DOPS20 do not display any significant coverage with actin, independent of the ion concentration. Second, the presence of divalent ions reverses these trends: whereas increasing concentrations of $MgCl_2$ increasingly suppress the ability of DOTAP20 to immobilize the filaments on its surface, the interaction of DOPC100

and DOPS20 with actin filaments is enhanced, although the adsorption on DOPC100 remains relatively low. For the highest salt concentration, one can clearly observe a prominent adsorption of F-actin to the negatively charged lipid bilayer, whereas the positive and neutral bilayer are only weakly covered.

It is worth noting that all of these experiments were done on supported lipid bilayers, where the supporting substrate can sometimes influence membrane fluidity or induce compositional asymmetry between the two leaflets (63–65). We therefore also performed some qualitative experiments where we eliminated the solid support and worked with giant unilamellar vesicles (GUVs) instead (see *SI Appendix*, Fig. S1 and Movies S1–S6). To assess actin adhesion to these free-standing membranes, we coated polystyrene beads with F-actin and pushed them against the GUV membranes using optical tweezers. By pulling the beads back from the GUV, we could directly test whether the membrane adhered to the actin-covered beads. Again, this showed the same trends: positively charged membranes in predominantly monovalent buffers strongly adhered to the beads, while negatively charged ones did not. In predominantly divalent buffer conditions, the DOPS and DOPC membranes displayed a moderate adhesion to the GUVs, which is consistent with the observations on supported bilayers.

Discussion and Conclusion

For F-actin in a buffer with monovalent ions, the results of our CG simulations are in line with our experimental data: we observe that actin filaments have a strong tendency to adsorb to positively charged bilayers, whereas they do not display an affinity to anionic membranes. The attachment to the neutral bilayer in simulations is weaker than to the cationic one, in line with the experimental observations.

With respect to cationic bilayers, we find in our simulations that G-actin is not immobilized on the surface but transiently adsorbs. This observation is true over a wide range of POTAP concentrations as well and explains previous fluorescence measurements showing the absence of G-actin on cationic monolayers (16). In the vast majority of occasions, G-actin adsorption takes place via the "front" surface of actin that contains the strongly negatively charged N terminus. In the actin filament, this surface is facing outward and has been identified to sequester calcium ions in actin bundles (22). The binding of actin to the positively charged membrane via the N terminus is furthermore similar to the attachment of the prokaryotic actin analog MreB to *Echerichia coli* membranes, which is realized by an amphiphilic helix that is located at the N terminus of the protein as well. A different, more persistent, conformation in which the binding takes place via the slow growing end of actin was detected in some cases, especially for larger POTAP concentrations.

The observation that G-actin only binds membranes transiently helps to explain the experimentally detected catalytic growth of F-actin on cationic membranes under buffer conditions that were otherwise unsuitable (8): the authors of ref. 8 claim that the origin of the filament formation is G-actin adsorption to the bilayer and subsequent in-plane (two-dimensional) assembly of filaments (Fig. 5*B*, *Left*). Our results, however, imply that actin monomers are not strongly attached to the bilayer but are oriented in a way that facilitates the formation of the filament (Fig. 5*B*, *Right*). In this context, the occasionally observed second binding mode could be of some importance for the formation of an F-actin nucleus as it orients G-actin in a way that exposes the fast-growing end. Since the growth direction is however facing away from the bilayer, it is unlikely to facilitate growth of the filament beyond its initial assembly. As the majority of monomers are still mobile and can approach the prealigned G-actin units in their preferred orientation, this mechanism can explain how actin is still able to form well-ordered helical filaments near the cationic bilayer (8, 17). By contrast, in the adsorption scenario, the motion of the actin units is restricted to a plane, which would likely cause the filaments to be more disordered.

An interesting microscopic detail identified in our simulation is the average distance between the actin filaments and POPC100

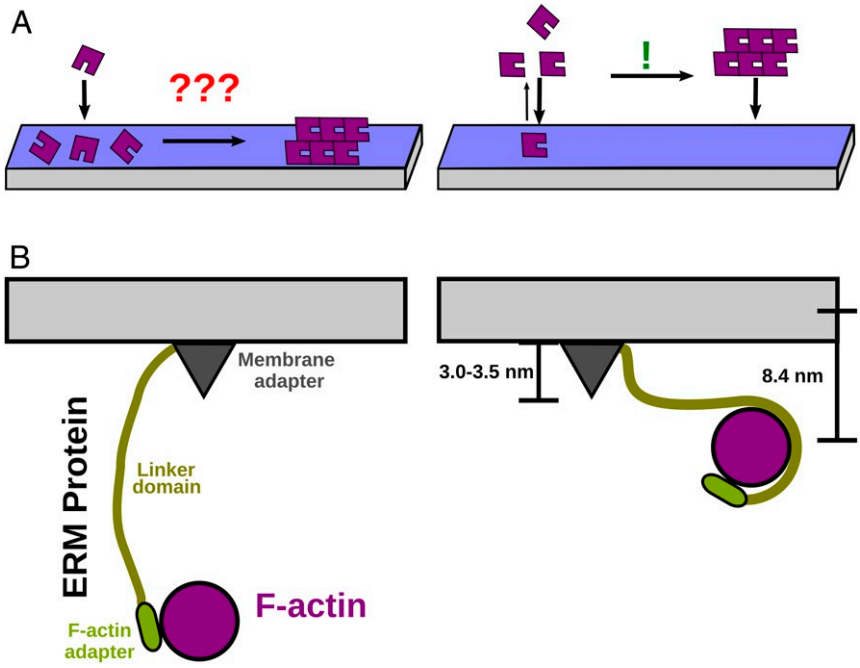

Fig. 5. Schematic interactions of actin and different membranes. (*A*) Mechanism of F-actin (purple) formation in the presence of a positively charged bilayer (blue). (*A*, *Left*) Mechanism suggested in ref. 8. (*A*, *Right*) Mechanism suggested by our simulations. (*B*) Lateral view on the possible arrangement of plasma membrane (light gray), ERM protein (shades of green), and F-actin (purple): with the linker domain of the ERM protein acting as a "fishing line" (*Left*) and with the linker domain wrapping around F-actin (*Right*).

and POPS20: while the distances differ only by roughly 1 nm, we find that F-actin controls the curvature of POPC100 but not of POPS20. This observation implies a critical distance of the respective centers of geometry between 7.4 and 8.4 nm, beyond which actin filaments are able, without any linker proteins, to bend the underlying bilayer. Increasing the separation of F-actin POPC100 above 7.5 nm demonstrates indeed that the shape control becomes less efficient. Furthermore, we find that F-actin, although not being adsorbed, still resides relatively close to the negatively charged bilayer. Since this distance range is consistent with the interaction length scale of the actin cortex with the inner leaflet of the plasma membrane of a cell, our findings strongly suggest that membrane interactions of actin may affect the anchoring function of actin–membrane linker proteins. For example, atomic force microscopy revealed that the membrane adapter of ERM proteins, the primary anchors for the actin cortex, extends 3.0 to 3.5 nm from the surface of a lipid bilayer into the buffer (66), whereas the linker domains of these proteins can reach up to 25 nm (24). The arrangement of the plasma membrane, ERM proteins, and F-actin is often depicted in a way that the filament is quite distant from the membrane and the linker of the ERM protein acts a "fishing line" for the actin filament (Fig. 5*B*, *Left*). Our results imply, however, that, despite the electrostatic repulsion, the actin filament can still approach negatively charged bilayers up to relatively close distances. Such a positioning would be consistent with small-angle neutron-scattering results that suggest the linker part of ERM proteins is partially wrapping around actin (67) rather than dangling in the cytosol (Fig. 5*B*, *Right*).

Finally, we studied the different binding properties of G- and F-actin in relation to the nature of the buffer cations. We found that the presence of divalent ions can alter the binding affinity of G-actin, which we can explain due to the very high affinity of the magnesium ions to the protein, in particular to the negatively charged N terminus, that effectively shield the negative charges of actin from interacting with the bilayers. In the case of POTAP20, this leads to an impairment of the transient adsorption of G-actin to the cationic membrane. For F-actin, we find both in simulation and experiment that an increasing concentration of divalent ions reduces the affinity of actin for the cationic lipid bilayer, whereas the affinity to anionic bilayers is enhanced. Based on the in silico results, we suggest a scenario where the divalent ions act as a molecular glue between the negatively charged filament and bilayer. This observation is reminiscent of the action of divalent cations as bundling agents for actin filaments (19–22).

In eukaryotic cells, there exist several control mechanisms to either suppress the amount of divalent ions in the presence of F-actin (35) or sever actin filaments (37) and avoid repolymerization (32, 36) in the presence of divalent ions. The existence of the ion-mediated direct binding of actin filaments may be one of the reasons why cells developed these functionalities, especially considering the fact that direct binding of cortical proteins can be observed in prokaryotic cells (68, 69). On the other hand, for the de novo design of synthetic cells, direct actin binding may be utilized for the construction of artifical cell cortices (39). Our findings suggest two routes that can be explored: a potential plasma membrane could either contain cationic lipids in absence of divalent ions or anionic lipids in the presence of divalent ions. In both cases, the control of the ion concentration can be used to modulate the adsorption between the cortex and the membrane, hence allowing tuning of the rigidity and, potentially, the shape of the cell.

In summary, our in vitro and in silico results highlight the importance of electrostatic interactions on the actin–membrane binding process. Both the composition of the bilayer and the nature of buffer ions are thereby of crucial relevance. Our simulations indicate that these trends are more pronounced for actin filaments than for actin monomers, which may impact the mechanism of filament formation in the presence of lipid bilayers.

Materials and Methods

Computational Methods. The MD simulations discussed throughout this article are based on the Martini force field (52, 53). The main concept of the Martini model is the mapping of on average four atoms (except for hydrogen) on one CG bead. The nonbonded interactions of the beads are determined by classifying the fragments inside each bead according to their chemical nature, e.g., polar, nonpolar, charged (see refs. 52 and 53 for details). This model has been extensively tested in a variety of situations (53).

The model for the G-actin was based on the Martini force field for proteins (70–72). Due to the anticipated importance of electrostatic interactions between actin and the lipid bilayer, the polarizable variant of the force field (Martini 2.1P) was chosen (72, 73). The structure of the monomeric G-actin containing ATP was adapted from the crystal structure of Graceffa and Dominguez (74) (Protein Data Bank [PDB] ID code 1nwk). The protein was completed by reconstructing the missing terminal residues (residues 1 to 5 and 372 to 375) as random coils with the program pymol (75) and transferring the coordinates of the DNase-binding loop (residues 40 to 57), that was not present in the 1nwk structure, from the structure of the actin–DNase I complex (PDB ID code 1atn) (76). An elastic network with a force constant of $k = 500$ kJ $\cdot$ mol $\cdot$ nm^{-2} was applied in between not chemically linked backbone beads within a cutoff of $r_C = 0.7$ nm to avoid unfolding of the molecule. Thereby, both the remodeled termini and the flexible DNase-binding loop were excluded to avoid a possible bias from the reconstruction. For the units in F-actin, the actin conformation reported by Oda et al. (77), which is based on X-ray refraction experiments on actin filaments, was used, while the force field parameters were the same as for G-actin; this model has been widely used a starting structure in MD simulation of F-actin (45, 47, 50, 51). No additional elastic network was introduced between the units of actin in the filament.

To test the mechanical and structural properties of our F-actin model, we computed the rise r and the twist angle τ between adjacent subunits as well as the persistence length l_p of the filament by applying the procedures detailed in refs. 41 and 78. The rise $r = 2.71$ nm $\pm$ 0.14 nm and the twist angle $\tau = -166.22^\circ \pm 3.94^\circ$ were in line with experimental observations ($r = 2.76$ nm and $\tau = -166.6^\circ$) (79) over the course of the simulations. The persistence length $l_p = 7.0 \pm 3.0$ μm is also consistent with prior experimental measurements of F-actin in the absence of phalloidin stabilization ($\sim$8 to 9 μm; ref. 80).

Each actin unit possesses a posttranslational modification, a methylation of His73 (MeHis73). Additionally, the nucleotide ATP is bound in the center of the molecule, next to a divalent cation (Ca^{2+} in the crystal structure, Mg^{2+} in biological situations). Since both can have an effect on the electrostatic properties of the molecule, we decided to model them explicitly in the CG model for actin: for MeHis73, the CG bead representing the methylation site was replaced by a charged bead (SQ0:+1), and the lengths of bonds connected to this bead were slightly increased. The model of ATP (together with its hydrolyzed counterpart ADP) was originally designed for this work. The mapping of the molecule was based on the recently published Martini model for RNA (81), and the bonded parameters were determined such that they reproduce a dataset of more than 500 structures from the PDB in which the respective nucleotide was cocrystallized. ATP and divalent ion, represented by a Qd:+2 bead (60), were eventually attached to the actin unit by a set of harmonic bonds that inhibit dissociation from the protein. A detailed description of the mapping and the parameterization of both MeHis73 and ATP (and ADP), as well as a list of the bonds that have been used to stabilize the cofactors in actin, can be found in *SI Appendix* and Datasets S1 and S2. Together with the MeHis73, ATP, and the divalent ion, each actin unit possessed a net charge of $q = -14e$.

The lipid bilayers consisted of the zwitterionic lipid POPC (net charge $q = 0$), the anionic POPS ($q = -1e$), and the cationic POTAP ($q = +1e$). The parameters for POPC and POPS were obtained from ref. 82 and have been widely studied for a large variety of different bilayers and membranes (53, 55, 83). The model for POTAP was varied from the model of DOTAP (84) by replacing the lipid tails with 1-palmitoyl-2-oleoyl, in analogy to the other lipids. The differences between the different lipids are thus only the different head groups.

For the F-actin simulations, a 26-unit filament has been created according to the model of Oda et al. (77), which represents a full turn of the helical polymer. The filament was placed parallel to the x axis in a

71.5 × 20 × 25 nm^3 box, where the *x* length was chosen such that the ends of the filament could interact with each other across the periodic boundaries; this effectively created the model of an infinite filament. A lipid bilayer was built in the *xy* plane with the tool insane.py (82) and placed $dz = 10$ nm away from the filament. An overview of the simulation setup can be seen in *SI Appendix*, Fig. S7*A*. Analogously, the G-actin system was built by placing a single actin unit 7.5 nm apart from a lipid bilayer in a 15 × 15 × 15 nm box (*SI Appendix*, Fig. S7*B*). After hydration (see below), the systems contained 765,000 (F-actin simulations) or rather 70,000 particles (G-actin simulations). We restricted our simulations of the filaments to actin units containing ATP rather than ADP. The reason for this is that there is some controversy on whether the DNase-binding loop is folded to a helix or stays disordered (44), which can alter the properties of the filament (45, 85, 86). Since proteins in the Martini force field have a fixed secondary structure, this may create an unrealistic bias. However, because simulations of G-actin containing ADP displayed the same adsorption behavior as their ATP counterpart (*SI Appendix*, Fig. S4*B*), we would expect a similar agreement for ADP-containing filaments as well.

In this work, three different bilayer compositions were studied: 100% POPC, 80% POPC + 20% POPS, and 80% POPC + 20% POTAP, hereafter referred to as POPC100, POPS20, and POTAP20, respectively. The systems underwent and energy minimization for 100 steps (only F-actin) by using the steepest descent algorithm. Thereafter, they were hydrated with a buffer of polarizable water (73) and 150 mM monovalent KCl ions, additional to the amount of ions that was needed to neutralize the charges of the filament and the membrane. To test the impact of the nature of the buffer ions on the adsorption behavior, we created systems that contained 75 mM $MgCl_2$ instead of 150 mM KCl; these systems are referred to as POPC100Mg75, etc. The number of positive charges in the buffer is thus the same for both kinds of systems, and only the type of cations was changed. Compared to the cytosol (c[Ca^{2+}] = 0.1 to 1.0 μM; ref. 32), this concentration of dialvent ions is relatively high. However, since divalent ions, like calcium, have a very high affinity to negatively charged membranes (33), the local ion concentration in the vicinity of the plasma membrane is much higher than the average cytosolic one, in line with our simulations and experiments. The effects of ions on the properties of lipid bilayers are, even in atomistic simulations, notoriously difficult to describe (34, 87); however, the Martini model has been found to describe complex ion-induced processes like membrane fusion (60). Furthermore, as the interplay between the ions and actin is of central importance for this work, we explicitly compared the distribution of the Mg^{2+} ions around G-actin of our CG model with an atomistic one (*SI Appendix*, Fig. S6). Although some differences exist, especially in the region around the flap (residue 236 to 251), we still observe a very good agreement between both resolutions.

After another energy minimization for 250 (F-actin)/1,000 (G-actin) steps, the system was equilibrated for 20 ns (both F- and G-actin) under constant volume and temperature conditions (NVT) at 300 K, where constant temperature conditions were achieved by coupling the system to a velocity-rescaling thermostat (88). The G-actin systems underwent additionally a subsequent equilibration for 500 ns under constant pressure and temperature conditions (NPT), thereby using the same thermostat as during the NVT equilibration as well as a pressure-rescaling barostat (89) with a time constant $\tau_p = 3$ ps and a isothermal compressibility $\beta = 3 \cdot 10^{-4} \cdot \text{bar}^{-1}$ that was coupled to the system in a semiisotropic way to achieve a constant pressure of 1 bar. During the equilibration, the backbone beads of actin were restrained by a harmonic potential with a force constant of $k = 500\ \text{kJ} \cdot \text{mol} \cdot \text{nm}^{-2}$. The production run was conducted for 1 (F-actin)/10 (G-actin) μs at a constant temperature $T = 300$ K and pressure P = 1 bar. For the production run, the Parrinello–Rahman thermostat (90, 91) was used ($\tau_p = 12$ ps; $\beta = 3 \cdot 10^{-4} \cdot \text{bar}^{-1}$) that was coupled in a anisotropic (F-actin) or semiisotropic (G-actin) manner to the system. In the case of F-actin, three replicas were simulated for POPC100, POPS20, and POTAP20. The G-actin simulations were simulated for a longer time, as we anticipated a more dynamic behavior of the monomers and intended to observe multiple (>1,000) binding and unbinding events. All simulations were performed with the program package gromacs-2016.5 (92). The simulation parameters were chosen according to the "new" parameters for Martini simulations (93). Notably, the electrostatic interactions were, as usual for polarizable Martini (73), treated with a cutoff potential and a dielectric constant of 2.5. The visualization of the molecules was done with the program VMD (94). The numerical analysis of data were carried out with the built-in routines of gromacs and the MDAnalysis program package (95, 96). The models and parameters of actin that were used for this work are available at http://cgmartini.nl/index.php/example-applications2/peptides.

Experimental Methods.

Protein preparation. Unlabeled monomeric actin from rabbit skeletal muscle was purchased from Hypermol. The lyophilized powder was resuspended following the supplier's instructions, and subsequently dialyzed into G-buffer—5 mM tris(hydroxymethyl)aminomethane (Tris)·HCl (pH 7.8), 0.1 mM $CaCl_2$, 0.2 mM ATP, 1 mM dithiothreitol (DTT)—to remove residual disaccharides from the freeze-drying process. The dialyzed protein was centrifuged at 120,000 × *g* for 3 h to remove any aggregates and then aliquoted, snap-frozen, and stored at −80 °C. Fluorescent actin was prepared by purifying actin from rabbit skeletal muscle and labeling the monomers with Alexa Fluor 649 carboxylic acid succinimidyl ester (97). Both labeled and unlabeled G-actin solutions were cleared before use to remove any aggregates. This was done by thawing the protein, leaving it on ice overnight, and subsequently centrifuging the solution at 120,000 × *g* for 20 min.

Sample preparation. All actin was polymerized under the same conditions: first, a mix of 10 mol % labeled and 90 mol % unlabeled actin monomers was prepared in G-buffer. Polymerization was then induced by adding a concentrated salt solution to obtain F-buffer conditions (20 mM Tris·HCl [pH 7.4], 50 mM KCl, 2 mM $MgCl_2$, 0.5 mM ATP, 1 mM DTT). Polymerization at an actin concentration of 30 μM and in the presence of 30 μM phalloidin (Sigma-Aldrich) to stabilize the filaments was allowed to progress for 1 h at room temperature in the dark, and the polymerized mix was stored on ice from then on for a maximum of 3 d. The different salt conditions were achieved by diluting the F-actin mix into the appropriate buffers, which were supplemented with 10 mM protocatechuic acid (PCA) and 0.5 μM protocatechuate-3,4-dioxygenase (PCD) to minimize photobleaching (98). We used the same G-actin stocks throughout and handled the polymerized actin with blunt-cut pipette tips to prevent filament breakage during handling and thus ensure a reproducible length distribution.

SUV preparation. Lipids—18:1 DOPC, DOPS, DOTAP, and 1,2-dioleoyl-*sn*-glycer-3-phosphoethanolamine-*N*-(lissamine rhodamine B sulfonyl) (rhodamine-PE)—were purchased from Avanti Polar Lipids. Stock solutions of the lipids were prepared in chloroform and stored at −20 °C. To prepare the lipid mixes, appropriate amounts of lipid stocks were pipetted into a small volume of chloroform in a glass tube and mixed by swirling. Three lipid mixes were used: DOPC/rhodamine-DOPE (99.95:0.05 molar ratio), DOPS/DOPC/rhodamine-DOPE (20:79.95:0.05 molar ratio), and DOTAP/DOPC/rhodamine-PE (20:79.95:0.05 molar ratio). The chloroform was evaporated under a gentle nitrogen flow while the tube was continuously turned around a tilted axis. This ensured that a homogeneous thin layer of lipids was deposited on the glass tube walls. To remove any remaining chloroform, the tubes were kept under vacuum overnight. The fully dried lipid films were rehydrated for 20 min in a buffer containing 20 mM imidazole (pH 7.4) and 50 mM KCl to a final lipid concentration of 1.25 mg/mL. Subsequently, the lipid film was detached from the glass tubes by vigorous vortexing. The mix, which was now opaque and slightly pink, was then transferred to a 1.5-mL Eppendorf tube and sonicated for 2 h in a Bandelin Sonoplus HD2070.2 sonicator equipped with a BR30 cup resonator. To avoid excessive heating of the lipid solution, the sonication was pulsed in a 15 s on/30 s off rhythm. After sonication, the clear solution contains small unilamellar vesicles (SUVs). SUV solutions were kept at room temperature for a maximum of 1 wk.

Channel preparation. Glass flow channels were prepared following a published protocol (97). In brief, glass microscopy slides and coverslips were cleaned with base piranha, and flow channels were prepared by sandwiching strips of parafilm between the slide and coverslip. Immediately after preparing the flow channels, they were loaded with the SUV suspensions and left to incubate for at least 10 min in a dark and humid environment to allow for the formation of a supported lipid bilayer. All channels were subsequently flushed with 10 channel volumes (CVs) of F-buffer (20 mM Tris·HCl [pH 7.4], 50 mM KCl, 2 mM $MgCl_2$) to remove any superfluous SUVs. The buffer in each channel was then replaced in a stepwise manner: first, 5 CVs of the target buffer without any proteins were flushed through. Secondly, this was replaced by 2 CVs of the target buffer including the photoprotective PCA/PCD mix. Finally, 1.5 CV of the sample, including the photoprotective mix and 2 μM filamentous actin, was loaded into the channel, and the channel was closed with vacuum grease to prevent evaporation. We allowed for an incubation time of at least 4 h between loading the sample and imaging, to ensure sufficient time for actin filament adsorption. All samples were kept at room temperature and in the dark.

Microscopy and image analysis. Dual-color TIRF images were taken on a Nikon Eclipse Ti-E inverted microscope equipped with a Roper TIRF module, a QuantEM:512SC electron-multiplying charge-coupled device camera, and an Apo TIRF 100× 1.49 NA oil immersion objective. In TIRF illumination conditions, fluorescent objects are only visible if they reside in the evanescent laser field, which decays within <100 nm above the glass surface. This ensures that we detect only actin filaments that are adsorbed to the lipid bilayers. The imaging settings were kept constant across all experiments. At least 20 images were acquired at random locations throughout each channel. For each condition, at least 4 separate channels from at least 2 independent experiments were imaged, leading to a minimum of 80 images per condition. Image processing was performed in a semi-automated manner: first, all images were inspected and discarded if the membrane showed any defects, or if a diffuse background fluorescence was present in the actin channel. All remaining images were processed automatically using a custom-written Python script. Images were first cropped to leave only the in-focus and homogeneously illuminated central area of the image (300 × 300 pixels) for analysis. The images were then denoised and binarized. Details on this procedure are given in *SI Appendix* and illustrated in *SI Appendix*, Fig. S2. The number of bright pixels was then used as a measure for the amount of actin adsorbed to the membrane in each image.

ACKNOWLEDGMENTS. We thank M. Kuit-Vinkenoog for the purification and fluorescent labeling of actin and A. Szuba, P. C. T. Souza, J. Barnoud, and M. J. Tadema for many helpful remarks on this work. Furthermore, we acknowledge the valuable remarks by the anonymous referees of this paper. We acknowledge the financial support of European Molecular Biology Organization Grant ALTF 1340-2016 and The Netherlands Organization for the Advancement of Science, within the framework of the Graduate Program Synthetic Biology and by the "BaSyC – Building a Synthetic Cell" Gravitation grant (024.003.019) of the Netherlands Ministry of Education, Culture and Science (OCW) and the Netherlands Organisation for Scientific Research. S.J.M. acknowledges funding from the European Research Council, through Advanced Grant "COMP-MIC-CROW-MEM."

1. T. D. Pollard, Actin and actin-binding proteins. *Cold Spring Harbor Perspect. Biol.* **8**, a018226 (2016).
2. T. D. Pollard, J. A. Cooper, Actin, a central player in cell shape and movement. *Science* **326**, 1208–1212 (2009).
3. L. Blanchoin, R. Boujemaa-Paterski, C. Sykes, J. Plastino, Actin dynamics, architecture, and mechanics in cell motility. *Physiol. Rev.* **94**, 235–263 (2014).
4. T. M. Svitkina, Ultrastructure of the actin cytoskeleton. *Curr. Opin. Cell Biol.* **54**, 1–8 (2018).
5. J. Stricker, T. Falzone, M. L. Gardel, Mechanics of the F-actin cytoskeleton. *J. Biomech.* **43**, 9–14 (2010).
6. G. Salbreux, G. Charras, E. Paluch, Actin cortex mechanics and cellular morphogenesis. *Trends Cell Biol.* **22**, 536–545 (2012).
7. G. G. Borisy, T. M. Svitkina, Actin machinery: Pushing the envelope. *Curr. Opin. Cell Biol.* **12**, 104–112 (2000).
8. A. Laliberte, C. Gicquaud, Polymerization of actin by positively charged liposomes. *J. Cell Biol.* **106**, 1221–1227 (1988).
9. L. Limozin, M. Bärmann, E. Sackmann, On the organization of self-assembled actin networks in giant vesicles. *Eur. Phys. J. E* **10**, 319–330 (2003).
10. A. X. Li, X. Q. Cui, F. Yang, X. R. Yang, Interaction between F-actin and negatively charged lipids membrane. *Chin. J. Anal. Chem.* **37**, 25–29 (2009).
11. F. C. Tsai, B. Stuhrmann, G. H. Koenderink, Encapsulation of active cytoskeletal protein networks in cell-sized liposomes. *Langmuir* **27**, 10061–10071 (2011).
12. F. C. Tsai, G. H. Koenderink, Shape control of lipid bilayer membranes by confined actin bundles. *Soft Matter* **11**, 8834–8847 (2015).
13. G. Li, Q. Wen, J. X. Tang, Single filament electrophoresis of F-actin and filamentous virus fd. *J. Chem. Phys.* **122**, 104708 (2005).
14. K. A. Taylor, D. W. Taylor, Formation of 2-D paracrystals of F-actin on phospholipid layers mixed with quaternary ammonium surfactants. *J. Struct. Biol.* **108**, 140–147 (1992).
15. A. Renault *et al.*, Surface-induced polymerization of actin. *Biophys. J.* **76**, 1580–1590 (1999).
16. B. Demé, D. Hess, M. Tristl, L. T. Lee, E. Sackmann, Binding of actin filaments to charged lipid monolayers: Film balance experiments combined with neutron reflectivity. *Eur. Phys. J. E* **2**, 125–136 (2000).
17. G. C. L. Wong *et al.*, Hierarchical self-assembly of F-actin and cationic lipid complexes: Stacked three-layer tubule networks. *Science* **288**, 2035–2039 (2000).
18. S. Garg, J. Tang, J. Rühe, C. Naumann, Actin-induced perturbation of PS lipid–cholesterol interaction: A possible mechanism of cytoskeleton-based regulation of membrane organization. *J. Struct. Biol.* **168**, 11–20 (2009).
19. J. X. Tang, P. A. Janmey, The polyelectrolyte nature of F-actin and the mechanism of actin bundle formation. *J. Biol. Chem.* **271**, 8556–8563 (1996).
20. M. Streichfuss *et al.*, Measuring forces between two single actin filaments during bundle formation. *Nano Lett.* **11**, 3676–3680 (2011).
21. X. Yu, A. Carlsson, Multiscale study of counterion-induced attraction and bundle formation of F-actin using an ising-like mean-field model. *Biophys. J.* **85**, 3532–3543 (2003).
22. T. E. Angelini, H. Liang, W. Wriggers, G. C. L. Wong, Like-charge attraction between polyelectrolytes induced by counterion charge density waves. *Proc. Natl. Acad. Sci. U.S.A.* **100**, 8634–8637 (2003).
23. G. van Meer, D. R. Voelker, G. W. Feigenson, Membrane lipids: Where they are and how they behave. *Nat. Rev. Mol. Cell Biol.* **9**, 112–124 (2008).
24. R. G. Fehon, A. I. McClatchey, A. Bretscher, Organizing the cell cortex: The role of ERM proteins. *Nat. Rev. Mol. Cell Biol.* **11**, 276–287 (2010).
25. A. Bretscher, K. Edwards, R. G. Fehon, ERM proteins and merlin: Integrators at the cell cortex. *Nat. Rev. Mol. Cell Biol.* **3**, 586–599 (2002).
26. S. Bosk, J. A. Braunger, V. Gerke, C. Steinem, Activation of F-actin binding capacity of ezrin: Synergism of PIP2 interaction and phosphorylation. *Biophys. J.* **100**, 1708–1717 (2011).
27. Q. Lubart *et al.*, Role of phosphorylation in moesin interactions with PIP2-containing biomimetic membranes. *Biophys. J.* **114**, 98–112 (2018).
28. J. A. Braunger *et al.*, Phosphatidylinositol 4,5-bisphosphate alters the number of attachment sites between ezrin and actin filaments: A colloidal probe study. *J. Biol. Chem.* **289**, 9833–9843 (2014).
29. Y. Senju *et al.*, Mechanistic principles underlying regulation of the actin cytoskeleton by phosphoinositides. *Proc. Natl. Acad. Sci. U.S.A.* **114**, E8977–E8986 (2017).
30. P. A. Janmey, R. Bucki, R. Radhakrishnan, Regulation of actin assembly by PI(4,5)P2 and other inositol phospholipids: An update on possible mechanisms. *Biochem. Biophys. Res. Commun.* **506**, 307–314 (2018).
31. Y. Senju, P. Lappalainen, Regulation of actin dynamics by pi(4,5)p2 in cell migration and endocytosis. *Curr. Opin. Cell Biol.* **56**, 7–13 (2019).
32. P. K. Hepler, The cytoskeleton and its regulation by calcium and protons. *Plant Physiol.* **170**, 3–22 (2016).
33. C. G. Sinn, M. Antonietti, R. Dimova, Binding of calcium to phosphatidylcholine–phosphatidylserine membranes. *Colloids Surf. A* **282-283** (suppl. C), 410–419 (2006).
34. J. Melcr, T. Mendes Ferreira, P. Jungwirth, O. H. S. Ollila, Improved cation binding to lipid bilayer with negatively charged POPS by effective inclusion of electronic polarization. *J. Chem. Theor. Comput.* **16**, 738–748 (2020).
35. L. Vanagas *et al.*, Differential effects of G- and F-actin on the plasma membrane calcium pump activity. *Cell Biochem. Biophys.* **66**, 187–198 (2013).
36. C. Revenu *et al.*, Villin severing activity enhances actin-based motility in vivo. *Mol. Biol. Cell* **18**, 827–838 (2007).
37. A. Prescott, J. Comerford, R. Magrath, N. Lamb, R. Warn, Effects of elevated intracellular magnesium on cytoskeletal integrity. *J. Cell Sci.* **89**, 321–329 (1988).
38. S. K. Vogel, F. Heinemann, G. Chwastek, P. Schwille, The design of macs (minimal actin cortices). *Cytoskeleton* **70**, 706–717 (2013).
39. Y. Mulla, A. Aufderhorst-Roberts, G. H. Koenderink, Shaping up synthetic cells. *Phys. Biol.* **15**, 041001 (2018).
40. W. Wriggers, K. Schulten, Investigating a back door mechanism of actin phosphate release by steered molecular dynamics. *Proteins Struct. Funct. Bioinf.* **35**, 262–273 (1999).
41. J. W. Chu, G. A. Voth, Allostery of actin filaments: Molecular dynamics simulations and coarse-grained analysis. *Proc. Natl. Acad. Sci. U.S.A.* **102**, 13111–13116 (2005).
42. P. Dalhaimer, T. D. Pollard, B. J. Nolen, Nucleotide-mediated conformational changes of monomeric actin and Arp3 studied by molecular dynamics simulations. *J. Mol. Biol.* **376**, 166–183 (2008).
43. T. Splettstoesser, F. Noé, T. Oda, J. C. Smith, Nucleotide-dependence of G-actin conformation from multiple molecular dynamics simulations and observation of a putatively polymerization-competent superclosed state. *Proteins: Struct. Funct. Bioinf.* **76**, 353–364 (2009).
44. J. Pfaendtner, D. Branduardi, M. Parrinello, T. D. Pollard, G. A. Voth, Nucleotide-dependent conformational states of actin. *Proc. Natl. Acad. Sci. U.S.A.* **106**, 12723–12728 (2009).
45. J. Pfaendtner, E. Lyman, T. D. Pollard, G. A. Voth, Structure and dynamics of the actin filament. *J. Mol. Biol.* **396**, 252–263 (2010).
46. S. Matsushita, T. Adachi, Y. Inoue, M. Hojo, M. Sokabe, Evaluation of extensional and torsional stiffness of single actin filaments by molecular dynamics analysis. *J. Biomech.* **43**, 3162–3167 (2010).
47. M. McCullagh, M. G. Saunders, G. A. Voth, Unraveling the mystery of ATP hydrolysis in actin filaments. *J. Am. Chem. Soc.* **136**, 13053–13058 (2014).
48. H. H. Katkar *et al.*, Insights into the cooperative nature of ATP hydrolysis in actin filaments. *Biophys. J.* **115**, 1589–1602 (2018).
49. J. W. Chu, G. A. Voth, Coarse-grained modeling of the actin filament derived from atomistic-scale simulations. *Biophys. J.* **90**, 1572–1582 (2006).
50. M. A. Deriu *et al.*, Multiscale modeling of cellular actin filaments: From atomistic molecular to coarse-grained dynamics. *Proteins Struct. Funct. Bioinf.* **80**, 1598–1609 (2012).
51. T. C. Bidone, T. Kim, M. A. Deriu, U. Morbiducci, R. D. Kamm, Multiscale impact of nucleotides and cations on the conformational equilibrium, elasticity and rheology of actin filaments and crosslinked networks. *Biomech. Model. Mechanobiol.* **14**, 1143–1155 (2015).
52. S. J. Marrink, H. J. Risselada, S. Yefimov, D. P. Tieleman, A. H. de Vries, The Martini force field: Coarse grained model for biomolecular simulations. *J. Phys. Chem. B* **111**, 7812–7824 (2007).
53. S. J. Marrink, D. P. Tieleman, Perspective on the Martini model. *Chem. Soc. Rev.* **42**, 6801–6822 (2013).

54. H. I. Ingólfsson, C. Arnarez, X. Periole, S. J. Marrink, Computational microscopy of cellular membranes. *J. Cell Sci.* **129**, 257–268 (2016).
55. S. J. Marrink *et al.*, Computational modeling of realistic cell membranes. *Chem. Rev.* **119**, 6184–6226 (2019).
56. A. Gautieri, A. Russo, S. Vesentini, A. Redaelli, M. J. Buehler, Coarse-grained model of collagen molecules using an extended Martini force field. *J. Chem. Theor. Comput.* **6**, 1210–1218 (2010).
57. S. Amir, M. Behzad, Nanomechanics of actin filament: A molecular dynamics simulation. *Cytoskeleton* **75**, 118–130 (2018).
58. F. Sun *et al.*, Molecular dynamics of the association of L-Selectin and FERM regulated by PIP2. *Biophys. J.* **114**, 1858–1868 (2018).
59. X. Yao, S. Grade, W. Wriggers, P. A. Rubenstein, His73, often methylated, is an important structural determinant for actin: A mutagenic analysis of His73 of yeast actin. *J. Biol. Chem.* **274**, 37443–37449 (1999).
60. M. Pannuzzo, D. H. De Jong, A. Raudino, S. J. Marrink, Simulation of polyethylene glycol and calcium-mediated membrane fusion. *J. Chem. Phys.* **140**, 124905 (2014).
61. V. Wollrab *et al.*, Polarity sorting drives remodeling of actin-myosin networks. *J. Cell Sci.* **132**, jcs219717 (2019).
62. M. P. Murrell, M. L. Gardel, F-actin buckling coordinates contractility and severing in a biomimetic actomyosin cortex. *Proc. Natl. Acad. Sci. U.S.A.* **109**, 20820–20825 (2012).
63. H. P. Wacklin, Composition and asymmetry in supported membranes formed by vesicle fusion. *Langmuir* **27**, 7698–7707 (2011).
64. A. Sonnleitner, G. Schütz, T. Schmidt, Free brownian motion of individual lipid molecules in biomembranes. *Biophys. J.* **77**, 2638–2642 (1999).
65. M. Przybylo *et al.*, Lipid diffusion in giant unilamellar vesicles is more than 2 times faster than in supported phospholipid bilayers under identical conditions. *Langmuir* **22**, 9096–9099 (2006).
66. V. Shabardina *et al.*, Mode of ezrin-membrane interaction as a function of PIP2 binding and pseudophosphorylation. *Biophys. J.* **110**, 2710–2719 (2016).
67. J. J. Jayasundar *et al.*, Open conformation of ezrin bound to PIP2 and to F-actin revealed by neutron scattering. *J. Biol. Chem.* **287**, 37119–37133 (2012).
68. J. Salje, F. vandenEnt, P. deBoer, J. Löwe, Direct membrane binding by bacterial actin MreB. *Mol. Cell* **43**, 478–487 (2011).
69. H. Shi, B. P. Bratton, Z. Gitai, K. C. Huang, How to build a bacterial cell: MreB as the foreman of E.coli construction. *Cell* **172**, 1294–1305 (2018).
70. L. Monticelli *et al.*, The Martini coarse-grained force field: Extension to proteins. *J. Chem. Theor. Comput.* **4**, 819–834 (2008).
71. X. Periole, M. Cavalli, S. J. Marrink, M. A. Ceruso, Combining an elastic network with a coarse-grained molecular force field: Structure, dynamics, and intermolecular recognition. *J. Chem. Theor. Comput.* **5**, 2531–2543 (2009).
72. D. H. de Jong *et al.*, Improved parameters for the Martini coarse-grained protein force field. *J. Chem. Theor. Comput.* **9**, 687–697 (2013).
73. S. O. Yesylevskyy, L. V. Schäfer, D. Sengupta, S. J. Marrink, Polarizable water model for the coarse-grained Martini force field. *PLoS Comput. Biol.* **6**, e1000810 (2010).
74. P. Graceffa, R. Dominguez, Crystal structure of monomeric actin in the ATP state: Structural basis of nucleotide-dependent actin dynamics. *J. Biol. Chem.* **278**, 34172–34180 (2003).
75. Schrödinger, LLC, *The PyMOL Molecular Graphics System* (Version 1.8.4, Schrödinger, LLC, New York, 2017).
76. W. Kabsch, H. G. Mannherz, D. Suck, E. F. Pai, K. C. Holmes, Atomic structure of the actin: DNase I complex. *Nature* **347**, 37–44 (1990).
77. T. Oda, M. Iwasa, T. Aihara, Y. Maeda, A. Narita, The nature of the globular- to fibrous-actin transition. *Nature* **457**, 441–445 (2009).
78. J. Fan, M. Saunders, G. Voth, Coarse-graining provides insights on the essential nature of heterogeneity in actin filaments. *Biophys. J.* **103**, 1334–1342 (2012).
79. T. Fujii, A. H. Iwane, T. Yanagida, K. Namba, Direct visualization of secondary structures of F-actin by electron cryomicroscopy. *Nature* **467**, 724–729 (2010).
80. H. Isambert *et al.*, Flexibility of actin filaments derived from thermal fluctuations. effect of bound nucleotide, phalloidin, and muscle regulatory proteins. *J. Biol. Chem.* **270**, 11437–11444 (1995).
81. J. J. Uusitalo, H. I. Ingólfsson, S. J. Marrink, I. Faustino, Martini coarse-grained force field: Extension to RNA. *Biophys. J.* **113**, 246–256 (2017).
82. T. A. Wassenaar, H. I. Ingólfsson, R. A. Böckmann, D. P. Tieleman, S. J. Marrink, Computational lipidomics with insane: A versatile tool for generating custom membranes for molecular simulations. *J. Chem. Theor. Comput.* **11**, 2144–2155 (2015).
83. H. I. Ingólfsson *et al.*, Computational lipidomics of the neuronal plasma membrane. *Biophys. J.* **113**, 2271–2280 (2017).
84. B. M. H. Bruininks, P. C. T. Souza, S. J. Marrink, A practical view of the Martini force field. *Biomol. Simul*. 105–127, (2019).
85. Z. A. O. Durer, K. Diraviyam, D. Sept, D. S. Kudryashov, E. Reisler, F-actin structure destabilization and DNase i binding loop fluctuations: Mutational cross-linking and electron microscopy analysis of loop states and effects on F-actin. *J. Mol. Biol.* **395**, 544–557 (2010).
86. G. M. Hocky *et al.*, Cations stiffen actin filaments by adhering a key structural element to adjacent subunits. *J. Phys. Chem. B* **120**, 4558–4567 (2016).
87. A. Catte *et al.*, Molecular electrometer and binding of cations to phospholipid bilayers. *Phys. Chem. Chem. Phys.* **18**, 32560–32569 (2016).
88. G. Bussi, D. Donadio, M. Parrinello, Canonical sampling through velocity rescaling. *J. Chem. Phys.* **126**, 014101 (2007).
89. H. J. C. Berendsen, J. P. M. Postma, W. F. van Gunsteren, A. DiNola, J. R. Haak, Molecular dynamics with coupling to an external bath. *J. Chem. Phys.* **81**, 3684–3690 (1984).
90. M. Parrinello, A. Rahman, Polymorphic transitions in single crystals: A new molecular dynamics method. *J. Appl. Phys.* **52**, 7182–7190 (1981).
91. S. Nosé, M. L. Klein, Constant pressure molecular dynamics for molecular systems. *Mol. Phys.* **50**, 1055–1076 (1983).
92. M. J. Abraham *et al.*, GROMACS: High performance molecular simulations through multi-level parallelism from laptops to supercomputers. *SoftwareX* **1**, 19–25 (2015).
93. D. H. de Jong, S. Baoukina, H. I. Ingólfsson, S. J. Marrink, Martini straight: Boosting performance using a shorter cutoff and GPUs. *Comput. Phys. Commun.* **199**, 1–7 (2016).
94. W. Humphrey, A. Dalke, K. Schulten, VMD: Visual molecular dynamics. *J. Mol. Graph.* **14**, 33–38 (1996).
95. N. Michaud-Agrawal, E. J. Denning, T. B. Woolf, O. Beckstein, MDAnalysis: A toolkit for the analysis of molecular dynamics simulations. *J. Comput. Chem.* **32**, 2319–2327 (2011).
96. R. J. Gowers *et al.*, "MDAnalysis: A Python package for the rapid analysis of molecular dynamics simulations" in *Proceedings of the 15th Python in Science Conference*, S. Benthall, S. Rostrup, Eds. (SciPy, Austin, TX, 2016), pp. 98–105.
97. J. Alvarado, G. H. Koenderink, "Chapter 6 - reconstituting cytoskeletal contraction events with biomimetic actin–myosin active gels" in *Building a Cell from its Component Parts, Methods in Cell Biology*, J. Ross, W. F. Marshall, Eds. (Academic Press, 2015), vol. 128, pp. 83–103.
98. C. E. Aitken, R. A. Marshall, J. D. Puglisi, An oxygen scavenging system for improvement of dye stability in single-molecule fluorescence experiments. *Biophys. J.* **94**, 1826–1835 (2008).